Thin-Walled Structures 174 (2022) 109094

Contents lists available at ScienceDirect

Thin-Walled Structures

journal homepage: www.elsevier.com/locate/tws

Full length article

Exact component-wise solutions for 3D free vibration and stress analysis of hybrid steel–concrete composite beams

J. Shen [a], A. Pagani [a,*], M.R.T. Arruda [b], E. Carrera [a]

[a] Mul^2 Team, Department of Mechanical and Aerospace Engineering, Politecnico di Torino, Corso Duca degli Abruzzi 24, 10129 Torino, Italy
[b] CERIS, Instituto Superior Técnico, Universidade de Lisboa, Portugal

ARTICLE INFO

Keywords:
Composite beams
Natural Frequency
Static analysis
Carrera Unified Formulation
High-order beam theories

ABSTRACT

This paper presents the analysis of free vibration and stress state of steel–concrete composite beams, using high-order theories and closed-form solutions based on Carrera unified formulation (CUF). The governing differential equations are formulated in terms of fundamental nuclei via CUF and the longitudinal differential problem is solved analytically by imposing simply supported boundary conditions. For the cross-sectional kinematics approximation, bilinear, cubic, and fourth-order Lagrange polynomials are adopted. In particular, the component-wise (CW) approach is applied in which the steel part and concrete part are considered as two independent components. To assess the efficiency of the proposed method, I-section and box-section composite beams are studied. The results are compared with those from other research and the commercial software ABAQUS. From accuracy, it is clear that, albeit the proposed approach is 1D, it can provide 3D accuracy, in terms of both free vibration and stress analysis of steel–concrete composite beams, with a significant reduction in the computational costs, which is innovative and worth promoting.

1. Introduction

Steel–concrete composite beams have been studied and analyzed by Mackay [1] since the early 20th century. These beams present some advantages when compared with traditional reinforced concrete or steel beams because composite beams possess light mass, high capacity, good ductility, and extra stiffness, which are all fundamental in structural design. Nowadays, they have been widely applied in civil engineering, mainly in building and bridge construction, assuming that there is a good connection between the I-section steel beam and the concrete slab. In any case, the analysis of these types of beams has been limited to either classical Euler–Bernoulli beam model (EBBM) [2], or Timoshenko beam model (TBM) [3,4], therefore, disregarding any transversal stress or strain effect in the structural design.

1.1. Literature review

Many refined beam theories have been proposed to overcome the shortcomings of classical beam models. A detailed review about modern theories for beam structures was recently published by Carrera [5]. For the sake of completeness, a brief overview and recent researches about beam theories are given here. Sokolnikoff [6], Wanger and Gruttmann [7–9] computed shear correction factors for several structural cases. Vlasov [10] introduced warping functions in modeling thin-walled beams and El Fatmi [11–13] has developed a non-uniform warping theory by introducing warping functions. The Generalized Beam Theory (GBT) proposed by Schardt and Heinz [14] is an alternative modeling concept that adds to Vlasov's model the distortion of the cross-section. Besides, many advanced beam models are based on the Saint-Venant solution. For example, Yoon [15] proposed a finite element formulation for nonlinear torsional analysis of 3D composite beams with the help of the Saint-Venant solution. Ladeveze [16] first introduced the Proper Generalized Decomposition method (PGD), which was applied to plate/shell problems by Bognet [17,18] and was extended to beams by Vidal [19]. Asymptotic methods are powerful tools and suitable to develop a structural model for thin-walled structures [20].

At present, free vibration analysis of concrete beams, which is quite significant for preventing resonance and damage of the beams, also begins to attract many researchers' concerns. Stefan [21] proposed three analytical models to study composite beams researched by Biscontin [22]. Two of them were based on EBBM, and the other used TBM. The result turned out TBM presented a better accuracy. Furthermore, Stefan [23] compared TBM with the rigid finite element method's (RFE) model and found TBM provides highly consistent results while a discrete RFE model is easy to build and modify. Recently, Niesterowicz [24] applied the same method based on TBM to vibration analysis of composite steel-polymer concrete box beams successfully.

To study the influence of shear connectors on natural frequency, Henderson [25] has done an experimental study with four types of

* Corresponding author.
E-mail address: alfonso.pagani@polito.it (A. Pagani).

https://doi.org/10.1016/j.tws.2022.109094
Received 1 October 2021; Received in revised form 15 February 2022; Accepted 18 February 2022
Available online xxxx

connectors and found larger values of connector stiffness resulted in lower natural frequencies. Meanwhile, Henderson [26] successfully modeled the steel–concrete composite beams with TBM. Besides, Huang and Su [27] presented analytical solutions for the dynamic response of composite beams with partial shear connections based on EBBT. Nguyen [28,29] proposed an analytical solution for the free vibration analysis of composite beams with interlayer slip based on the TBT. Xu and Wu [30] presented a two-dimensional (2D) analytical solution for the free vibration and buckling analysis of composite beams with interlayer slip based on TBT too.

Based on the Hamilton principle, Zhou [31] induced the governing differential equations and the corresponding boundary conditions of steel–concrete composite box girder with consideration of the shear lag effect, shear deformation, slip, as well as rotational inertia. In advance, Jiang and Zhou [32] also considered the above influencing factors and derived the improved steel–concrete composite box beam element stiffness and mass matrices. It turned out shear-lag effect, shear deformation, and rotational inertia all make the natural frequency higher. Lai and Feng [33,34] took the same method to analyze the natural vibration of steel–concrete composite truss beam and composite box beam with corrugated webs, respectively.

To overcome the limitations of classical beam models that cannot capture the higher-order manner of composite beam structures such as warping, in-plane distortion of cross-section, and shear effects, Chakrabarti [35] proposed a higher-order beam model considering partial shear interaction between the adjacent layers and the transverse shear deformation of the beam to predict the dynamic response of composite beams. Guanghui He [36] also proposed a new model for free vibration and buckling of composite beams with a higher-order beam theory.

Unlike the above publications, the Carrera unified formulation (CUF) is a hierarchical formulation that considers the order of the model as a free parameter, or an input, of the analysis [37]. In this regard, this theory can consider various structural problems with no need for ad hoc assumptions. Therefore, EBBM and TBM can be obtained as particular cases. CUF was introduced by Carrera et al. [38–40] for plates and shells and extended to beam structures by Carrera and Giunta [41] in 2010. The comprehensive discussion about CUF can be found in [37]. Over the past years, the CUF has been applied to different problems by the use of Taylor series polynomials as cross-sectional functions [42–44]. More recently, Lagrange polynomials have been used to discretize the cross-sectional kinematics [45,46]. It is worth noting that CUF also has been applied to free vibration analysis of different beams, including solid and thin-walled cross-sections beams, cross-ply laminated beam structures; e.g. [47–51]. In the recent literature, CUF has also been employed for the investigation of reinforced composite structures for civil engineering applications; e.g. [52,53].

1.2. Research significance

Previous works that studied the performance of steel–concrete composite beams have considered several influence factors, such as shear slip, shear lag effect, shear deformation. A steel–concrete composite beam consisting of the concrete slab and the I-section steel beam is a common research object which is also shown as Fig. 1(a). However, most of the mathematical models mentioned in the previous publications employ classical theories, which inevitably have assumptions and simplifications that may not be appropriate depending on the problem under consideration. In the present work, the use of exact solutions based on the component-wise (CW) approach (see Fig. 1(b)) is proposed, which has been demonstrated to be physically and geometrically consistent. In the CW approach, each component is modeled individually and simultaneously by using CUF beam elements (see [40]). Then, continuity conditions among the different components are automatically satisfied if Lagrange polynomials are used to approximate the cross-section kinematics. A recent successful application of the CW approach can be seen in [53]. The advantages and novelties of the proposed solutions are:

(1) There is no need to simplify the physical dimension of structures for the component-wise approach.
(2) CUF considers the order of the model as a free parameter of the analysis, which is easy to get enough accuracy as needed.
(3) Considering the simply-supported boundary conditions, the governing equation can be solved in an exact manner which is the quasi-exact Navier-type solution. This exact solution for free vibration and stress analysis of steel–concrete composite beams will be characterized by high efficiency in terms of computational costs and unprecedented accuracy.

According to the author's best knowledge, it is the first time applying CUF to simulate the composite concrete–steel structures numerically and calculate their eigenmodes in this work where a convergence study is investigated for the vibration modes, displacement, strain, and stress fields. The main novelty of this work is to provide a new advanced model for closed-form solutions of steel–concrete composite beams, which will provide a benchmark work for future research.

1.3. Organization

The paper is organized as follows: First, the Lagrange expansion (LE) CUF models is presented. Then, the governing differential equations of free vibration analysis and stress analysis with simply supported boundary conditions are discussed and their closed-form solutions are also given. Next, two examples taken from the literature are used to validate the proposed model. Their results are also compared with those from ABAQUS [54] to assess the availability of CUF to provide 3D accuracy of steel–concrete composite beams. Finally, some meaningful conclusions based on the above analysis are obtained.

2. Higher-order beam theory via CUF

By using the CUF, the three-dimensional (3D) displacement field of composite steel–concrete beams can be expressed as follows:

$$\mathbf{u}(x, y, z; t) = F_\tau(x, z)\mathbf{u}_\tau(y; t), \qquad \tau = 1, 2, \ldots, M \tag{1}$$

where F_τ varies within the cross-section; $\mathbf{u}_\tau$ is the generalized displacements vector and M stands for the number of terms in the expansion. According to the Einstein notation, the repeated subscript, τ, indicates summation. The choice of F_τ and M is arbitrary, that is, different base functions of any order can be taken into account to model the kinematic field of a beam above the cross-section [40].

In this paper, Lagrange polynomials are used for F_τ functions. Lagrange polynomials are usually given in terms of normalized coordinates and only three quadrilateral Lagrange polynomials, four-point (L4) bilinear, nine-point (L9) cubic, and 16-point (L16) fourth-order, are presented here.

The simplest quadrilateral Lagrange polynomial is the four-point (L4) and the interpolation functions are given by

$$F_\tau = \frac{1}{4}(1 + r\, r_\tau)(1 + s\, s_\tau), \qquad \tau = 1, 2, 3, 4 \tag{2}$$

where r and s are the normalized coordinates that vary from -1 to 1 and r_τ and s_τ are the actual coordinates of the four nodes.

Then, the interpolation functions of nine-point (L9) cubic polynomial element are given by

$$\begin{gathered} F_\tau = \frac{1}{4}(r^2 + r\, r_\tau)(s^2 + s\, s_\tau), \qquad \tau = 1, 3, 5, 7 \\ F_\tau = \frac{1}{2}s_\tau^2(s^2 + s\, s_\tau)(1 - r^2) + \frac{1}{2}r_\tau^2(r^2 + r\, r_\tau)(1 - s^2), \qquad \tau = 2, 4, 6, 8 \\ F_\tau = (1 - r^2)(1 - s^2), \qquad \tau = 9 \end{gathered} \tag{3}$$

where r_τ and s_τ are the actual coordinates of the nine nodes.

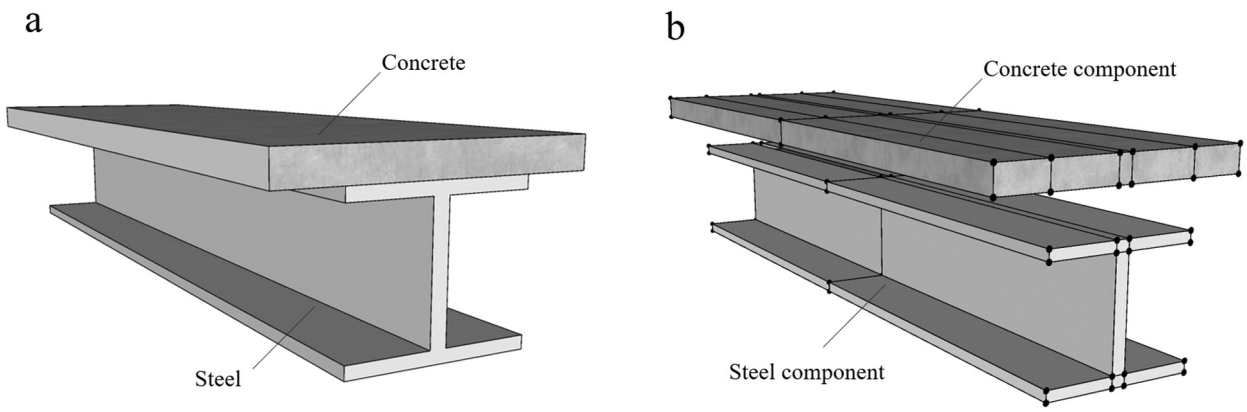

Fig. 1. Component-wise approach for a steel–concrete composite beam. (a) Composite beams; (b) Component-wise approach.

Finally, the interpolation functions of 16-point (L16) fourth-order polynomial element are given by

$$F_{\tau mn} = L_m(r)L_n(s), \qquad m,n = 1,2,3,4 \tag{4}$$

where

$$L_1(r) = \frac{1}{16}(r-1)(1-9r^2), \qquad L_2(r) = \frac{9}{16}(3r-1)(r^2-1)$$
$$L_3(r) = \frac{9}{16}(3r+1)(1-r^2), \qquad L_4(r) = \frac{1}{16}(r+1)(9r^2-1)$$

The cross-section displacement fields can be defined according to different elements and Eq. (1). For instance, the complete displacement field given by one single L4 element is

$$\begin{aligned} u_x(x,y,z) &= F_1(x,z)u_{x1}(y) + F_2(x,z)u_{x2}(y) + F_3(x,z)u_{x3}(y) + F_4(x,z)u_{x4}(y) \\ u_y(x,y,z) &= F_1(x,z)u_{y1}(y) + F_2(x,z)u_{y2}(y) + F_3(x,z)u_{y3}(y) + F_4(x,z)u_{y4}(y) \\ u_z(x,y,z) &= F_1(x,z)u_{z1}(y) + F_2(x,z)u_{z2}(y) + F_3(x,z)u_{z3}(y) + F_4(x,z)u_{z4}(y) \end{aligned} \tag{5}$$

where $u_{x1}(y), \ldots, u_{z4}(y)$ are the unknown variables of the problem and represent the translational displacement components of each of the four points of the L4 element. The above displacement variables are the only unknowns, which do not lie on the beam element axis.

3. Governing equations and closed-form solution

3.1. Governing equations

The adoption of LE models does not imply any formal changes in the problem governing equations which can be derived by means of the Principle of Virtual Displacements (PVD). According to the PVD, the following equation holds:

$$\delta L_{int} + \delta L_{ine} = \delta L_{ext} \tag{6}$$

where L_{int} is the internal elastic work, L_{ine} is the inertial work, L_{ext} is the work done by the external forces, and δ indicates the virtual variation.

The virtual variation of the internal elastic work is

$$\delta L_{int} = \int_V \delta\boldsymbol{\epsilon}^{\mathrm{T}}\boldsymbol{\sigma}\,\mathrm{d}V = \int_L \delta\mathbf{u}_s^{\mathrm{T}}\mathbf{K}^{\tau s}\mathbf{u}_\tau\,\mathrm{d}y + \left[\delta\mathbf{u}_s^{\mathrm{T}}\boldsymbol{\Pi}^{\tau s}\mathbf{u}_\tau\right]_{y=0}^{y=L} \tag{7}$$

where $\boldsymbol{\epsilon}$ is the strain vector, $\boldsymbol{\sigma}$ is the stress vector, $\mathbf{K}^{\tau s}$ is the linear differential stiffness matrix and $\boldsymbol{\Pi}^{\tau s}$ is the matrix of natural boundary conditions. Matrices are given in terms of 3 × 3 fundamental nuclei, which can be expanded automatically depending on the theory order [40].

The virtual variation of the inertial work is written as

$$\delta L_{ine} = \int_V \delta\mathbf{u}\rho\ddot{\mathbf{u}}\,\mathrm{d}V = \int_L \delta\mathbf{u}_s\mathbf{M}^{\tau s}\ddot{\mathbf{u}}_\tau\,\mathrm{d}y \tag{8}$$

where ρ is the material density, $\ddot{\mathbf{u}}$ is the second derivative of displacement $\mathbf{u}$ with respect to time t, and $\mathbf{M}^{\tau s}$ is the fundamental nucleus of the mass matrix.

The virtual work done by the external loads is

$$\delta L_{ext} = \int_V \delta\mathbf{u}^{\mathrm{T}}\mathbf{g}\,\mathrm{d}V + \int_S \delta\mathbf{u}^{\mathrm{T}}\mathbf{p}\,\mathrm{d}S + \int_L \delta\mathbf{u}^{\mathrm{T}}\mathbf{q}\,\mathrm{d}y + \delta\mathbf{u}^{\mathrm{T}}\mathbf{P} \tag{9}$$

where $\mathbf{g}$ are the volume forces, $\mathbf{p}$ are the surface forces, $\mathbf{q}$ are the line forces and $\mathbf{P}$ are the concentrated loads.

A undamped free vibration analysis investigates the equilibrium between elastic forces and inertial forces. Therefore, Eq. (6) can be written as:

$$\delta L_{int} = -\delta L_{ine} \tag{10}$$

Accounting for Eqs. (7) and (8), the governing differential equation of the free vibration analysis can be rewritten in the following compact form:

$$\delta\mathbf{u}_s : \mathbf{K}^{\tau s}\mathbf{u}_\tau = -\mathbf{M}^{\tau s}\ddot{\mathbf{u}}_\tau \tag{11}$$

The natural boundary conditions can be written as:

$$\delta\mathbf{u}_s : \left[\boldsymbol{\Pi}^{\tau s}\mathbf{u}_\tau\right]_{y=0}^{y=L} = 0 \tag{12}$$

In the case of static stress analysis, Eq. (6) can be simplified into:

$$\delta L_{int} = \delta L_{ext} \tag{13}$$

If only a surface loading is considered, the external virtual work Eq. (9) due to the pressure loading can be given by:

$$\delta L_{\mathrm{ext}} = \int_S \delta\mathbf{u}^{\mathrm{T}}\mathbf{p}\,\mathrm{d}S \tag{14}$$

Accounting for Eqs. (7) and (14), the governing differential equation of the static analysis can be rewritten in the following compact form:

$$\delta\mathbf{u}_s : \mathbf{K}^{\tau s}\mathbf{u}_\tau = \mathbf{p}^s \tag{15}$$

where $\mathbf{p}^s$ is the fundamental nucleus of the loading vector containing only surface pressures. The natural boundary conditions are the same as in Eq. (12).

For the sake of brevity, these matrices, such as $\mathbf{K}^{\tau s}$, $\mathbf{M}^{\tau s}$ and $\boldsymbol{\Pi}^{\tau s}$ are not given here but they can be found in [47,48]. Besides, the explicit expression of the Eq. (11), Eq. (12) and (15) can be found in [55]. Overall, any theory can be implemented as before in terms of the FNs by expanding them using the indexes τ and s.

3.2. Closed-form analytical solution

The Navier-type solution can be used to solve the static and free vibration problems using LE-based CUF theories. For doing this, the solution of the differential governing equations of free vibration problems

is supposed by imposing simply supported boundary conditions:

$$u_{x\tau}(y;t) = U_{x\tau}e^{i\omega t}\sin(\alpha y)$$
$$u_{y\tau}(y;t) = U_{y\tau}e^{i\omega t}\cos(\alpha y) \quad (16)$$
$$u_{z\tau}(y;t) = U_{z\tau}e^{i\omega t}\sin(\alpha y)$$

The term α in Eq. (16) is given by

$$\alpha = \frac{m\pi}{L} \quad (17)$$

where m represents the half-wave number along the beam axis. $U_{x\tau}, U_{y\tau}$ and $U_{z\tau}$ are the maximum displacement amplitudes function of the motion. ω is an arbitrary circular or angular frequency and i is the imaginary unit.

By substituting Eq. (16) into the equations of motion Eq. (11), the algebraic eigensystem in the compact form is obtained as:

$$\delta\mathbf{U}_s : (\overline{\mathbf{K}}^{\tau s} - \omega^2\overline{\mathbf{M}}^{\tau s})\mathbf{U}_\tau = 0 \quad (18)$$

where $\overline{\mathbf{K}}^{\tau s}$ and $\overline{\mathbf{M}}^{\tau s}$ are the fundamental nuclei of the algebraic stiffness and mass matrices, respectively. Considering the simply supported boundary condition, these matrices can be simplified as shown in the Appendix.

In the case of static problems, there is no need to consider time-dependent displacements. Therefore, the solution of the above differential governing equations is proposed as:

$$u_{x\tau}(y) = U_{x\tau}\sin(\alpha y)$$
$$u_{y\tau}(y) = U_{y\tau}\cos(\alpha y) \quad (19)$$
$$u_{z\tau}(y) = U_{z\tau}\sin(\alpha y)$$

Meanwhile, the external surface loadings varying along the beam axis y are proposed as:

$$\mathbf{p} = \left\{ p^{\pm}_{xx}\sin(\alpha y) \quad p^{\pm}_{xy}\cos(\alpha y) \quad p^{\pm}_{xz}\sin(\alpha y) \quad p^{\pm}_{zx}\sin(\alpha y) \right.$$
$$\left. \times \; p^{\pm}_{zy}\cos(\alpha y) \quad p^{\pm}_{zz}\sin(\alpha y) \right\}^{\mathrm{T}} \quad (20)$$

where $p^{\pm}_{xx}$, $p^{\pm}_{xy}$, …, $p^{\pm}_{zz}$ are the amplitudes of the surface loading. The sign $\pm$ means the positive value or the negative value. It depends on whether the surface loading shows the same orientation as the normal unit vector.

By substituting Eqs. (19) and (20) into Eq. (15), the algebraic system of equations of the generic simply supported beam subjected to pressure loads is obtained as:

$$\delta\mathbf{U}_s : \overline{\mathbf{K}}^{\tau s}\mathbf{U}_\tau = \overline{\mathbf{p}} \quad (21)$$

For the sake of brevity, $\overline{\mathbf{p}}$ is not shown here, but it can be found in [55]. The explicit expressions of Eqs. (18) and (20) can also be found in [49].

4. Free vibration analysis

To validate the accuracy of the present approach, two composite beams with different kinds of cross-section from [32,56] are analyzed here. The results from the LE closed-form solutions are compared with those from 3D solid models by using the commercial software ABAQUS [54]. The elastic material models for the steel and concrete are used in this work. Both concrete and steel materials are isotropic materials, and their constitutive relations are both based on a linear behavior. All of those models have the same boundary condition that is simply supported on both sides.

4.1. I-steel concrete composite beam

Fig. 2 shows the cross-section of a composite beam from [56]. The upper part is a concrete slab whose thickness is 0.05 m and width is 0.3 m, that is, $h_1 = 0.05$ m, $b_1 = b_2 = 0.1$ m. The lower part is a I-section steel whose dimension is $0.1 \times 0.1 \times 0.006 \times 0.008$ m, that is $t_1 = 0.008$ m, $t_2 = 0.006$ m, and $h_2 = 0.1$ m. Those two parts are connected by some studs in [56]. The length of total beam is 2 m. The relevant material properties are shown in Table 1.

Table 1
Material properties of I-steel concrete composite beam.

Material	Elastic modulus (GPa)	Poisson ratio	Mass density (kg/m^3)
Concrete	38.9	0.3	2500
Steel	210	0.2	7850

The LE cross-sectional discretizations with Lagrange elements are depicted in Fig. 2 for illustrative purposes. Fig. 2(b) and (d) show bilinear Lagrange elements. Fig. 2(c) and (e) show cubic Lagrange elements.

Table 2 shows the first 8 natural frequencies. The first row in Table 2 shows the 1st natural frequency from [56]. Various LE models are considered in the table and they are shown in rows 2–6. Results from various ABAQUS models are also shown in rows 7–9. Both the ABQ C3D8 model with 76 620 DOFs and the ABQ C3D20 model with 269880 DOFs have 13 750 elements. There are 103000 elements in the ABQ C3D8 model whose number of DOFs is 445824. Although the number of DOFs of the ABQ C3D20 model is only 269880, the ABQ C3D20 model shows better accuracy than the ABQ C3D8 model with 445824 DOFs does. Therefore, it turns out that taking quadratic order elements is more effective than only increasing the number of linear order elements. Furthermore, treating results from the ABQ C3D20 model as reference results is the best. However, considering that the differences among the three ABAQUS models are quite small, it is preferable to choose C3D8 elements in ABAQUS for further analysis to save computational costs.

From Table 2, [56] just calculated the first natural frequency of the composite beam considering no shear-slip effect. The value from [56] is the lowest comparing other results among the first frequencies, because Zhang [56] made calculations based on some assumptions, one of which is the plane section hypothesis. From rows 2 to 6, the 15L16 model always shows the best accuracy among five different LE models because it has enough DOFs. In the first four natural frequencies, the percentage differences between the L4 models and the ABQ C3D20 model are small. Starting from the 5th frequency, the L4 model cannot produce reasonable results anymore. Especially for the 6th frequency, the percentage difference of the 12L4 and 15L4 model from the ABQ C3D20 model are 243.43% and 202.07%, respectively. The reason the L4 model cannot give good results is that L4 models do not have enough DOFs to characterize the shell-like modes.

In addition, it is worth noting that although the 15L16 model can give better results than the C3D8 model, the results of the 15L9 model can also approach 3D results from ABAQUS. Therefore, the first eight modes attained from 15L9 models are depicted in Fig. 3. The first two modes are bending modes along x and y, respectively. The third mode is torsional mode and the fourth mode is also bending mode along x. The rest shows complex modes that the L4 model does not have enough DOFs to characterize. For comparison, the first eight modes from ABAQUS are also depicted in Fig. 4. Modes in Fig. 3 are quite similar to those in Fig. 4, which demonstrates the 3D capabilities of the present beam formulation. Therefore, the 15L9 model is sufficient and recommended in this case considering the balance between accuracy and computational costs.

4.2. Steel–concrete composite box-beam

A steel–concrete composite box beam is the other example from [32] that is considered for the assessment of the present beam model. The geometry of the cross-section is shown in Fig. 5. The values of parameters in Fig. 5 are: $b_1 = b_3 = 0.4$ m, $b_2 = 0.2$ m, $b_4 = 0.12$ m, $h_1 = 0.12$ m, $h_2 = 0.4$ m, $t_1 = 0.04$ m, $t_2 = t_3 = 0.025$ m. The length of total simply supported beam is 10 m. Table 3 lists the relevant material

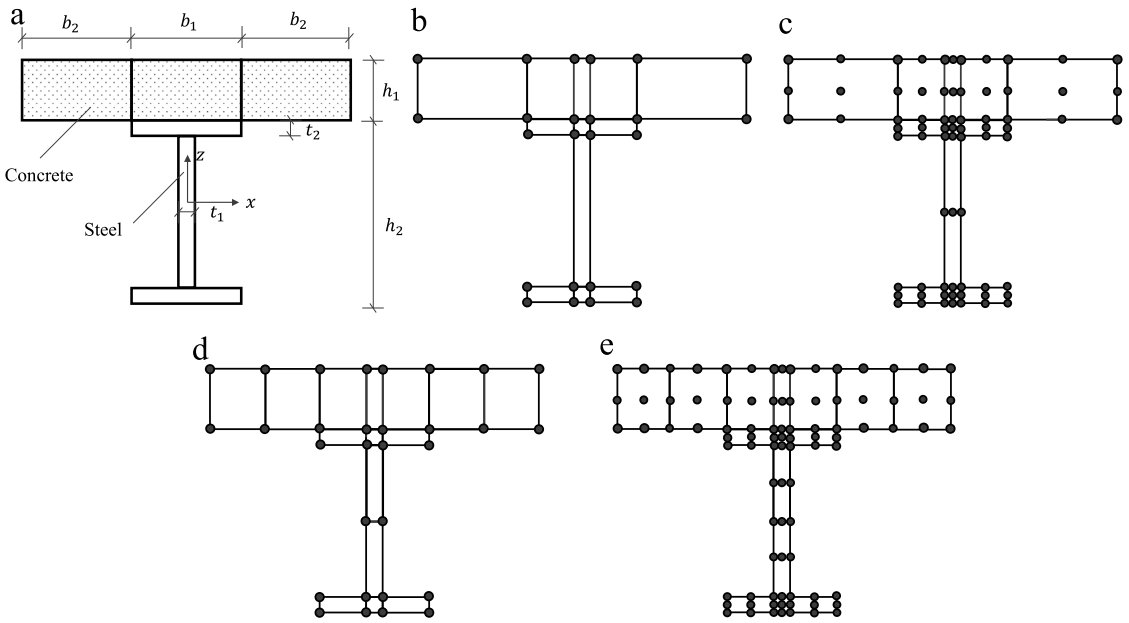

Fig. 2. I-girder cross-section and LE discretizations. (a) I-girder cross-section; (b) 12L4; (c) 12L9; (d) 15L4; (e) 15L9.

Table 2
Natural frequencies (Hz) of I-girder.

Model	DOFs	1st	2rd	3nd	4th	5th	6th	7th	8th
Zhang [56]	–	75.70	–	–	–	–	–	–	–
Present 12L4	72	78.41	112.61	225.73	283.64	411.37	1087.63	470.36	559.31
Present 15L4	90	78.28	112.26	220.01	282.89	402.90	958.99	461.63	556.98
Present 12L9	213	77.98	111.06	200.32	280.55	317.66	332.13	446.10	521.06
Present 15L9	267	77.97	110.79	196.74	280.42	308.81	322.10	445.75	517.28
Present 15L16	534	77.95	110.65	194.13	280.11	305.00	316.58	445.27	514.90
ABQ C3D8	76 620	78.09	110.84	195.42	281.20	307.35	318.99	445.19	516.37
ABQ C3D8	445 824	77.96	110.69	194.32	280.17	305.52	317.47	445.23	515.10
ABQ C3D20	269 880	77.94	110.64	194.01	279.97	304.91	316.70	445.22	514.62

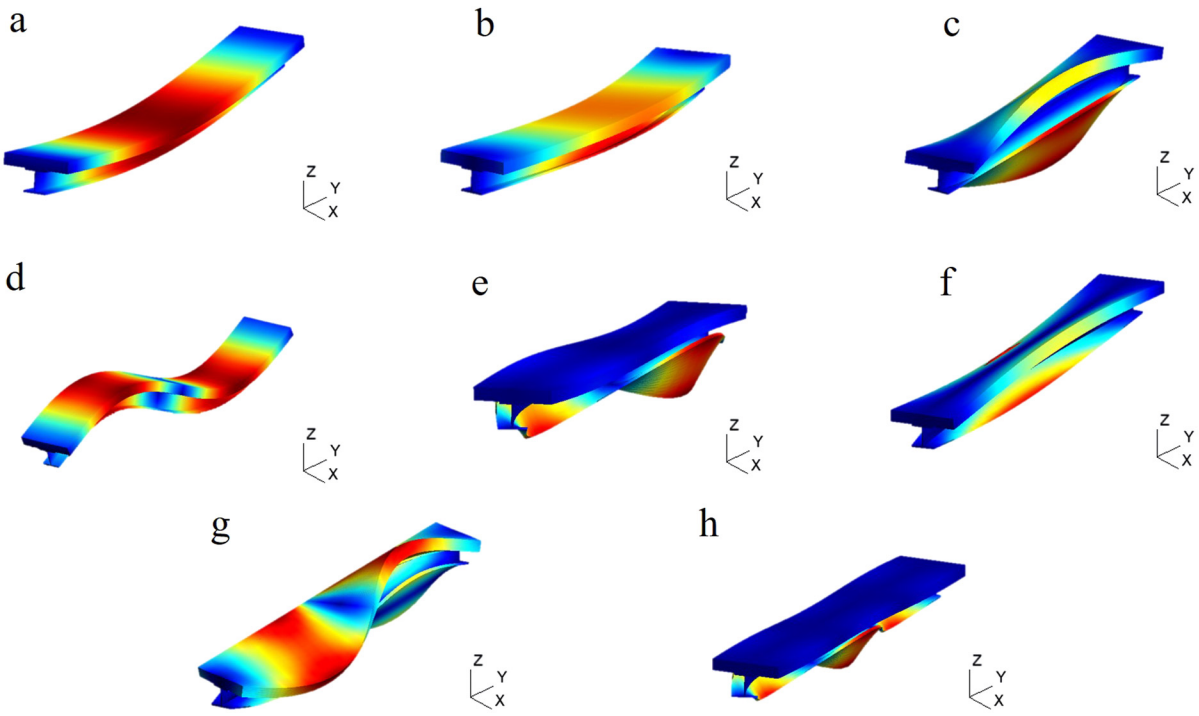

Fig. 3. First eight modes by the 15L9.(a) flexural mode, f = 77.97 Hz; (b) flexural mode, f = 110.79 Hz; (c) torsional mode, f = 196.74 Hz; (d) flexural mode, f = 280.42 Hz; (e) local torsional mode, f = 308.81 Hz; (f) shell-like mode, f = 322.10 Hz; (g) torsional mode, f = 445.75 Hz; (h) local torsional mode, f = 517.28 Hz.

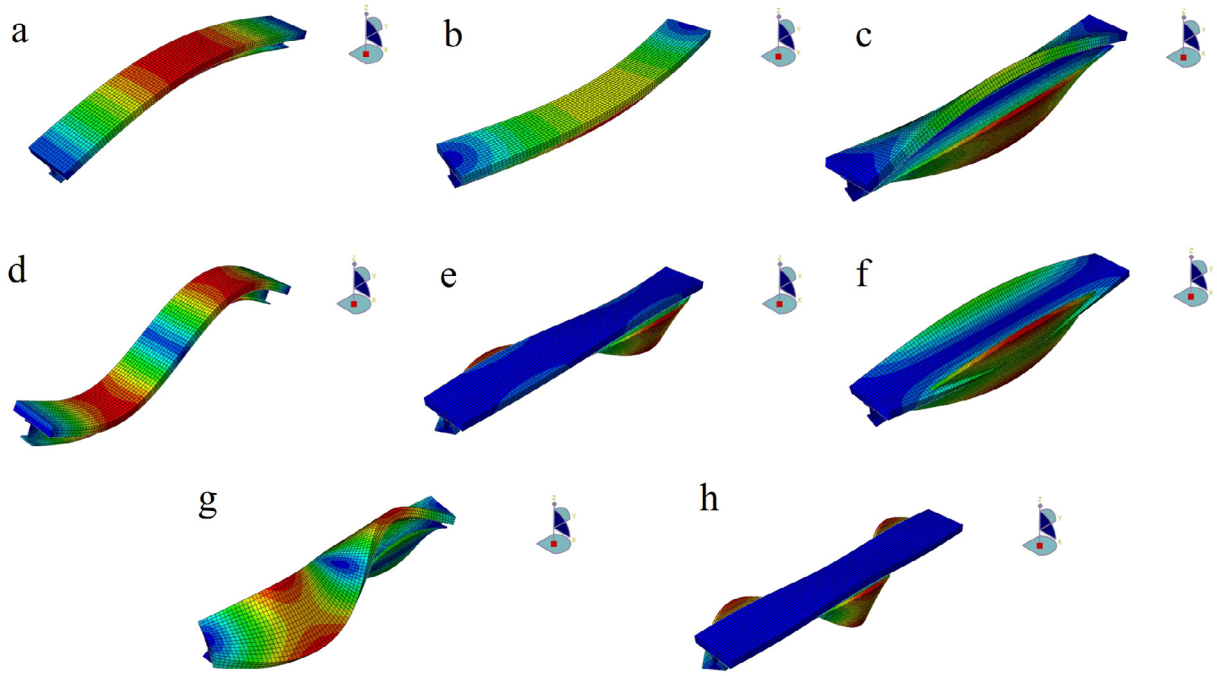

Fig. 4. First eight modes by the ABAQUS.(a) flexural mode, f = 77.94 Hz; (b) flexural mode, f = 110.64 Hz; (c) torsional mode, f = 194.01 Hz; (d) flexural mode, f = 279.97 Hz; (e) local torsional mode, f = 304.91 Hz; (f) shell-like mode, f = 316.70 Hz; (g) torsional mode, f = 445.22 Hz; (h) local torsional mode, f = 514.62 Hz.

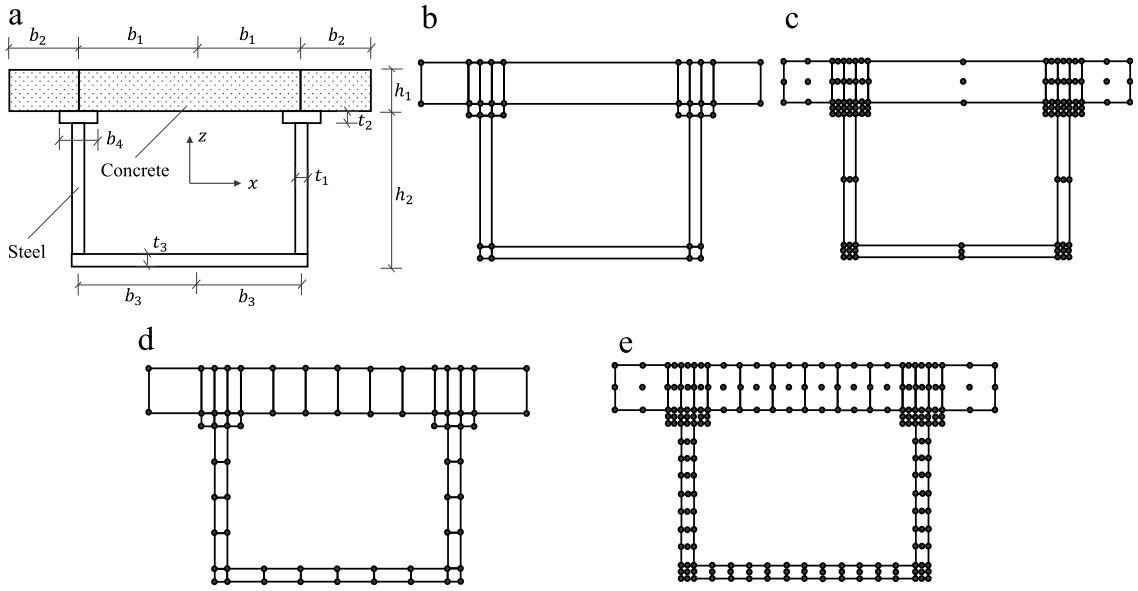

Fig. 5. Box-girder cross-section and LE discretizations.(a) Box-girder cross-section; (b) 20L4; (c) 20L9; (d) 36L4; (e) 36L9.

Table 3
Material properties of steel–concrete composite box-beam.

Material	Elastic Modulus (GPa)	Poisson ratio	Mass density (kg/m^3)
Concrete	45	0.28	2400
Steel	200	0.18	7900

properties. Various cross-sectional discretizations are shown in Fig. 5 for illustrative purposes.

Table 4 shows the flexural natural frequencies for the beam analyzed by [32], the present beam theories, and ABAQUS. m means the number of semi-waves. Zhou [32] improved stiffness and mass matrices considering many influencing factors based on a cubic Hermite polynomial shape function. However, his method is also based on some assumptions that the plane-section assumption is taken and lateral strain, bending of the slab, and shear deformation out of the plane of the slab are neglected. The above assumptions caused limitations of Zhou's method, which accounts for the difference between Zhou's results and LE models' results.

For the sake of brevity, only one ABAQUS model is introduced for comparison. Natural frequencies of LE models decrease with the increase of DOFs when m is fixed. When m equals 1, results from different models are similar. However, with the increase of m, the L16 model owns the best accuracy, and the L4 model shows the worse accuracy. Especially for 8 semi-waves, the result from 20L4 is nearly three times that of ABQ C3D8. The above phenomenon can be attributed to the increase in DOFs. The more DOFs the model has the better

Table 4
Natural frequency (Hz) of Box-girder.

Model	DOFs	m = 1	2	3	4	5	6	7	8
RFB [32]	–	17.71	43.93	80.09	124.48	175.85	–	–	–
Present 20L4	108	15.33	59.10	125.86	209.31	304.02	405.90	512.14	620.85
Present 36L4	204	15.21	58.23	122.54	200.16	283.02	361.91	423.13	457.49
Present 20L9	336	15.19	58.14	122.32	199.79	281.42	345.06	375.44	398.05
Present 36L9	624	15.19	57.80	118.74	175.19	198.02	207.50	214.89	222.27
Present 36L16	1260	15.18	57.75	118.22	171.70	191.83	200.67	207.85	215.15
ABQ C3D8	2 177 355	15.19	57.77	118.48	173.41	194.77	203.91	211.21	218.57

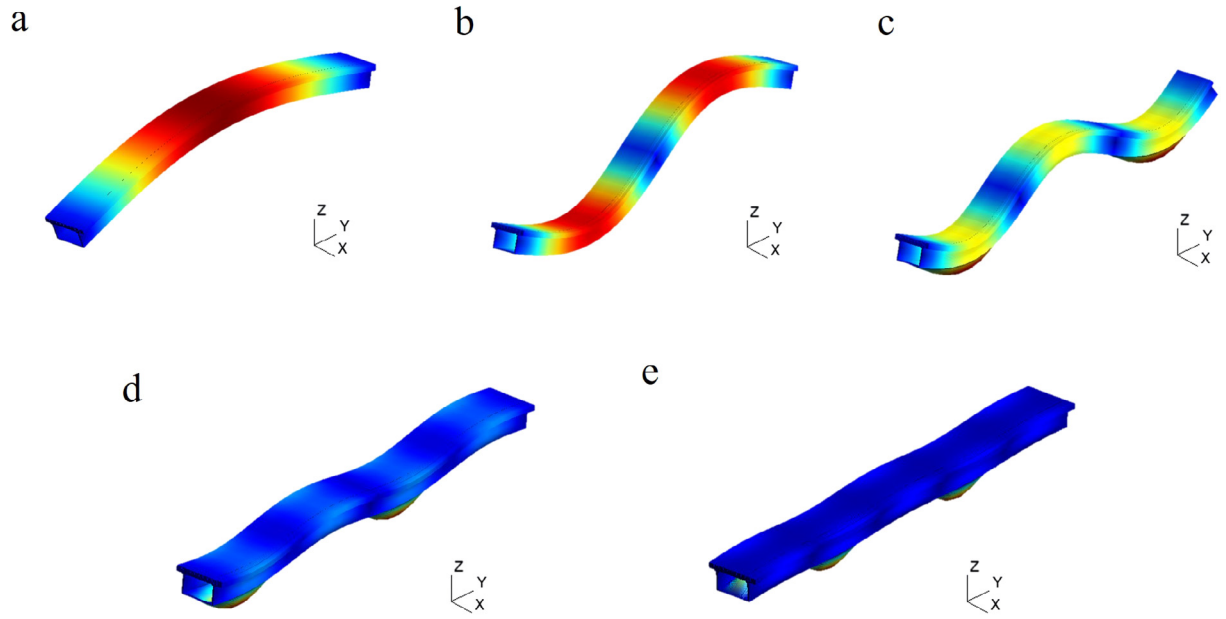

Fig. 6. First modes related to $m = 1 - 5$ of Box-girder cross-section by the 36L9 model.(a) $m = 1$, $f = 15.19$ Hz; (b) $m = 2$, $f = 57.80$ Hz; (c) $m = 3$, $f = 118.74$ Hz; (d) $m = 4$, $f = 175.19$ Hz; (e) $m = 5$, $f = 198.02$ Hz.

accuracy the result shows. Among all models, the natural frequencies of the 36L16 model are smaller than these of the ABAQUS model, which demonstrates the high efficiency of the L16 model. However, comparing results from the 36L9 model and ABAQUS model, the 36L9 model is powerful enough to show satisfactory results in free vibration analysis of steel–concrete composite box beams.

Figs. 6 and 7 show the modes from 36L9 and ABAQUS, respectively. The modes are flexural modes when m = 1 and 2 as shown in Fig. 6. When m equals 4 and 5, the flexural modes mainly occur locally in the steel part, which is not shown in Zhou's work [32]. Besides, it is worth noting modes in Figs. 6 and 7 are quite similar to each other, which demonstrates 36 L9 elements are effective enough for calculation. Furthermore, the phenomenon that the steel penetrates the concrete is shown in some modes, indicating that the reduction of scale factors is necessary.

5. Static stress analysis

To investigate the application of CUF in the static analysis, the above two kinds of composite beams, subjected to a stable pressure load, are also used to do stress analysis here. Assuming the beams are only under the pressure load that is on the top surface and along the y-axis. From Eq. (20), the load function in Fig. 8 is

$$p = p_{zz}^{-} \sin(\alpha y) \tag{22}$$

where p_{zz}^{-} is the maximum value in the mid-span, which is $10,000$ Pa.

For comparison, the displacements, normal stresses, and strains of the mid-span cross-section can be obtained from the above-proposed models and ABAQUS. Besides, shear stresses and strains of one-fifth span cross-section will also be obtained because shear stresses and strains are close to zero in the mid-span section. It is inconvenient to show all results on one cross-section. So, Fig. 9(a) and (b) choose one specific path to show curves of different results from I-girder and box-girder, respectively.

5.1. I-steel concrete composite beam

Fig. 10 shows the mid-span deflections, which are obtained from one path shown in Fig. 9(a). The path starts at the vertex of the axis of symmetry and ends at the bottom point of the axis of symmetry. In the beginning, only the ABAQUS model with coarse mesh is considered. Results from L4 models are much smaller than those from ABAQUS, while L9 and L16 show great results that are larger than those from ABAQUS. The reason for the above phenomenon is that the L4 model cannot provide enough DOFs, though 15L4 has more DOFs than 12L4 does. ABAQUS model cannot perform as well as 15L9 and 15L16 because there may be a convergence problem that can be handled by refining the mesh. To explain it, another ABAQUS model with finer mesh is conducted in Fig. 10. It turns out the ABAQUS model with finer mesh can produce a better result. Although both ABAQUS models cannot achieve the same accuracy as 15L9 and 15L16 do, the difference between ABAQUS models and 15L9 or 15L16 is within 0.2%. Considering that more and more refined mesh will lead to heavy computational costs, it is also preferable to treat results from the ABAQUS model with coarse mesh as the reference results for further analysis.

From Fig. 11, it is evident that the 12L4 model gives the wrong curves compared with other models. For the 15L4 model, a few points are not matched with other curves, but it gives a great trend. In general, the curves from 15L9 and 15L16 models match well with that from ABAQUS except when the true distance is around 0.05 m, which

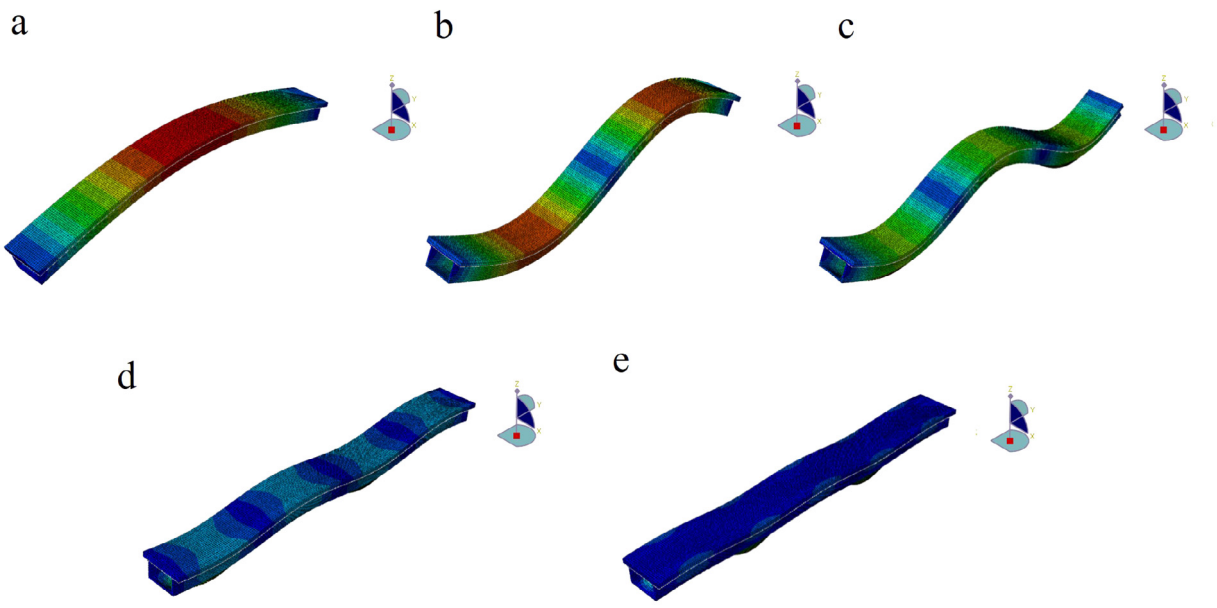

Fig. 7. First modes related to $m = 1 - 5$ of Box-girder cross-section by ABAQUS.(a) $m = 1$, $f = 15.19$ Hz.(b) $m = 2$, $f = 57.77$ Hz.(c) $m = 3$, $f = 118.48$ Hz.(d) $m = 4$, $f = 173.41$ Hz.(e) $m = 5$, $f = 194.77$ Hz.

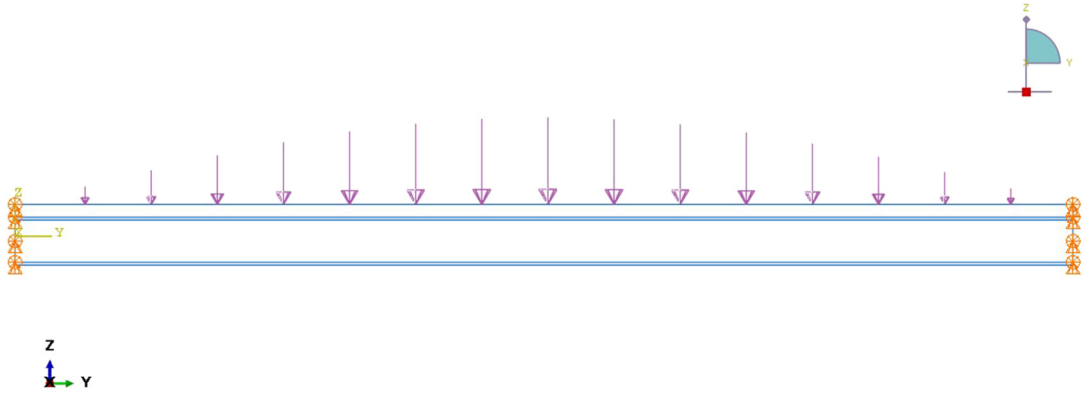

Fig. 8. Beams under pressure load.

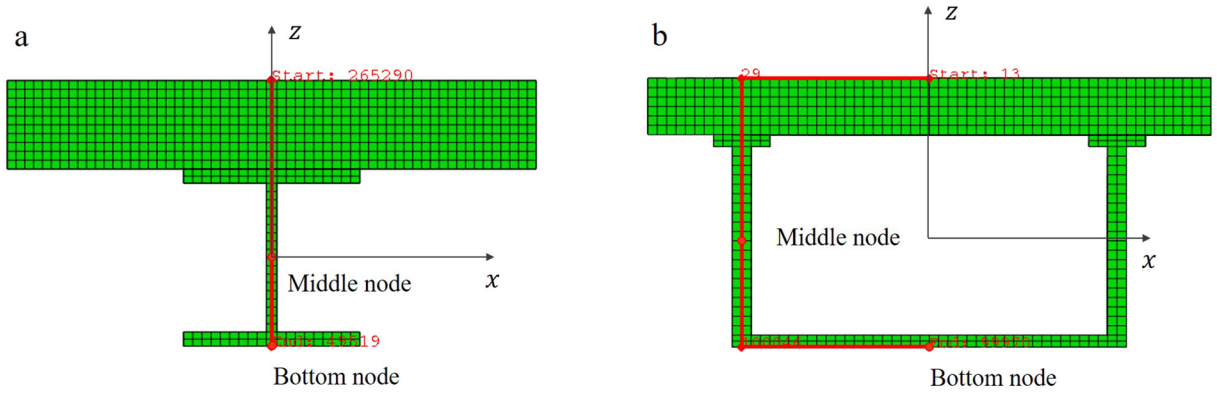

Fig. 9. Path and nodes on cross sections. (a) I-girder; (b) Box-girder.

indicates 15L9 and 15L16 models are effective in normal stress analysis. Considering 0.05 m is the point where there is an interface between steel and concrete, it is acceptable that results from ABAQUS are higher than those from 15L9 and 15L16, because the relationship between steel and concrete is not taken into account here.

In Fig. 12, Except for 12L4, the curves of other models are very consistent with the curve of the ABAQUS model. The normal strain is linear over the beam depth at mid-span from Fig. 12. 12L4 model cannot show the strain linearity for the lack of DOFs.

Fig. 13 shows the shear stresses at one-fifth span. Shear stresses mainly occur on the steel web. On the top concrete slab, shear stresses

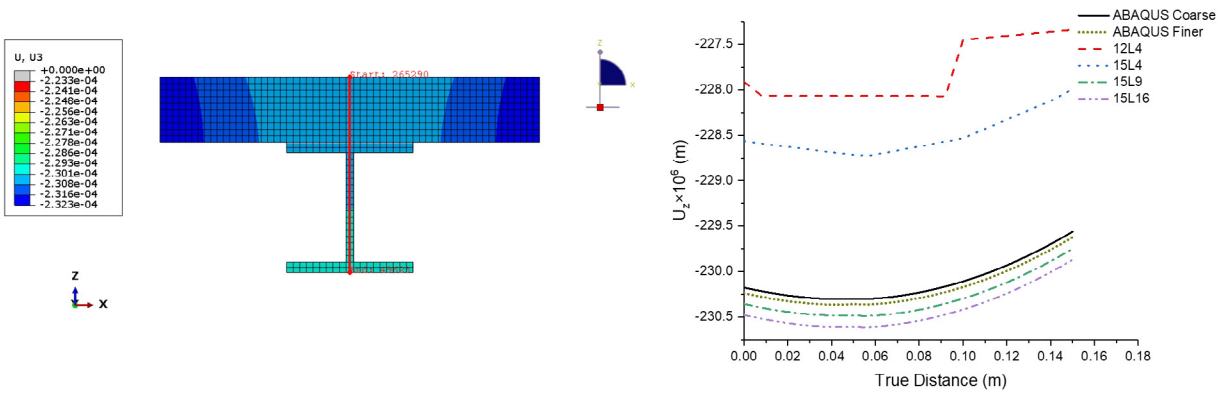

Fig. 10. Mid-span deflections along z-axis U_z according to different LE-CUF models and 3D ABAQUS.

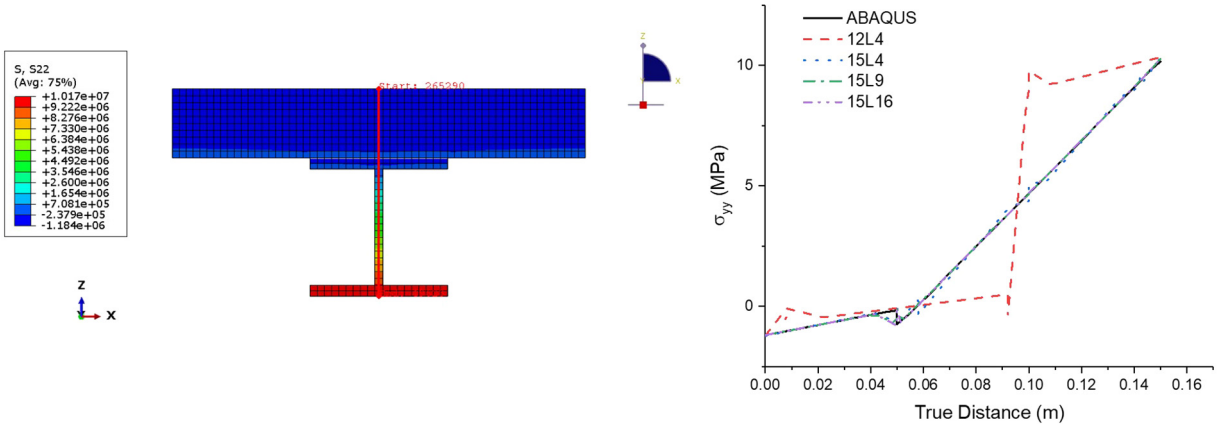

Fig. 11. Mid-span normal stresses σ_{yy} according to different LE-CUF models and 3D ABAQUS.

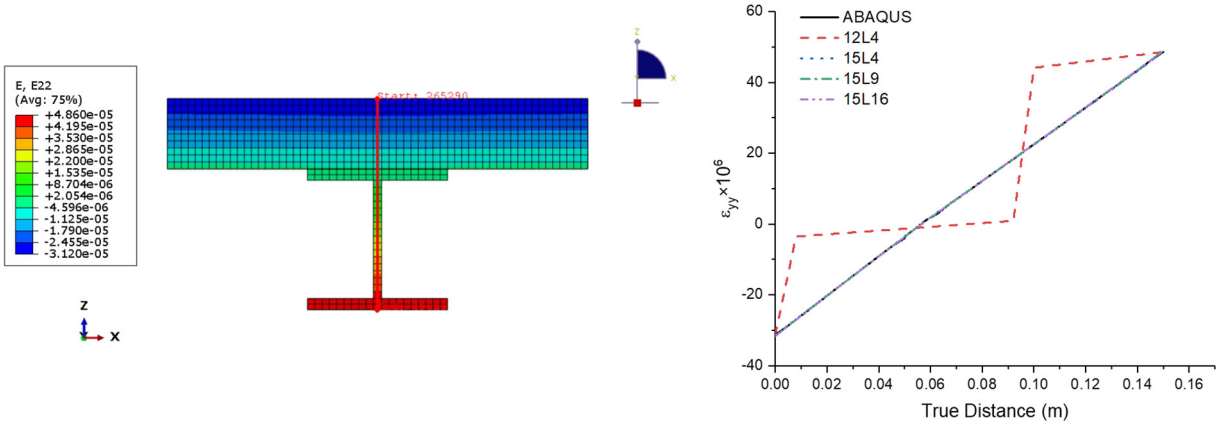

Fig. 12. Mid-span normal strains ϵ_{yy} according to different LE-CUF models and 3D ABAQUS.

are quite small or close to zero. From shear stress curves, two L4 models do not show great accuracy, while the curves of 15L9 and 15L16 can match with the curve of ABAQUS at most nodes.

The shear strain curves of different models at one-fifth span can be seen in Fig. 14. It is the same as shear stresses that shear strains mainly occur on the steel web. 12L4 and 15L4 models do not show great accuracy in shear strains. The strain curves of 15L9 and 15L16 are consistent with the curve of ABAQUS, except when the true distance is around 0.05 m where steel and concrete meet. This phenomenon is similar to that in Fig. 11 for the lack of consideration of the relationship between steel and concrete.

Table 5 shows different results obtained from different models and different cross-sections. Columns 3 to 5 mean mid-span deflections, normal stresses, and normal strains, respectively. They are all obtained from the bottom nodes which can be seen in Fig. 9(a). Columns 6 to 7 mean one-fifth span shear stresses and strains, respectively. They are all obtained from the middle nodes which can also be found in Fig. 9(a). In terms of all results in Table 5, the differences among 15L9, 15L16, and ABAQUS are quite small. Results of the 12L4 model are always quite away from these of ABAQUS because of the lack of enough DOFs.

Overall, Figs. 10–14 and Table 5 confirm the accuracy of all models except the 12L4 model in static analysis of composite I beam.

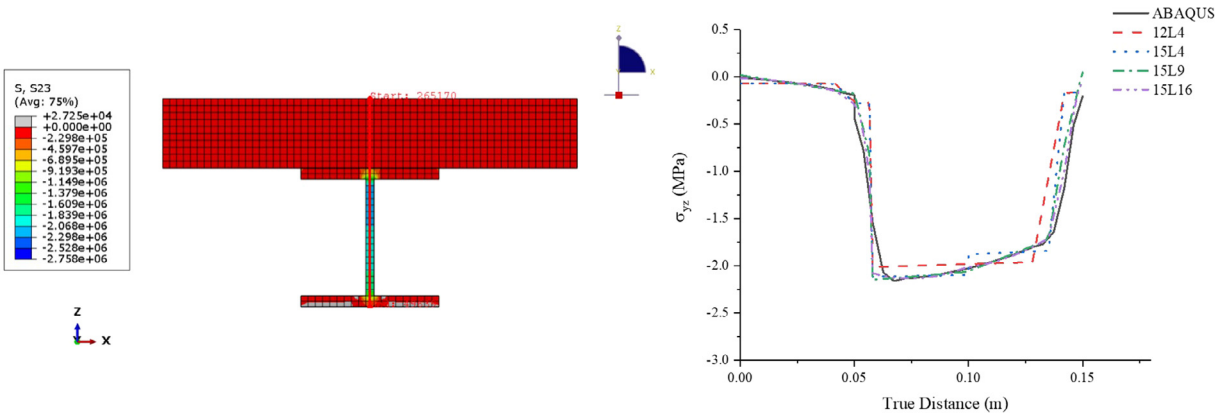

Fig. 13. One-fifth span shear stresses σ_{yz} according to different LE-CUF models and 3D ABAQUS.

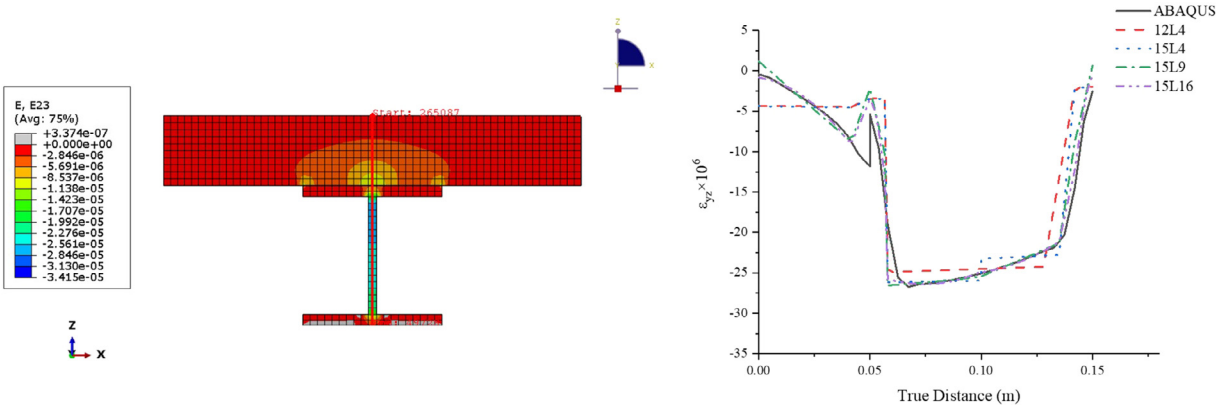

Fig. 14. One-fifth span shear strains ϵ_{yz} according to different LE-CUF models and 3D ABAQUS.

Table 5
Static results of steel–concrete composite I-beam.

Model	DOFs	U_z/mm	σ_{yy}/Mpa	$\epsilon_{yy} \times 10^6$	σ_{yz}/Mpa	$\epsilon_{yz} \times 10^6$
Present 12L4	72	−0.2273	10.3491	48.5698	−2.0022	−24.7886
Present 15L4	90	−0.2280	10.3221	48.7062	−2.1083	−26.2499
Present 15L9	267	−0.2297	10.2808	48.9882	−2.1202	−26.2499
Present 15L16	534	−0.2299	10.2809	48.9828	−2.1334	−26.4133
ABQ C3D8	1 020 144	−0.2296	10.1665	48.6015	−2.1339	−26.4192

5.2. Steel–concrete composite box-beam

Fig. 15 shows the mid-span deflections, which are obtained from one path shown in Fig. 9(b). The path starts at the vertex of the axis of symmetry, passes through the left steel web, and ends at the bottom point of the axis of symmetry. Results of 20L4 are the smallest among all models, indicating that 20L4 cannot present great accuracy in terms of mid-span deflections. At the starting point, results of 36L9 and 36L16 are close to that of ABAQUS. After that, the ABAQUS curve begins to approach the 36L4 model curve, which can be accounted for the convergence problem. The maximum difference between the ABAQUS model and the 36L16 model is around 0.3% that is quite small. Therefore, another ABAQUS model with refined mesh will not be shown here. 36L9 and 36L16 curves are close with each and they both show great accuracy in mid-span deflections.

From Fig. 16, it is clear that the normal stresses on the top concrete slab and bottom steel part are almost uniform. The phenomenon of shear lag is not obvious because the cantilever concrete part in the mid-span cross-section is small. The normal stress curves of all models show a huge increase at the interface of steel and concrete. It can be seen that all CUF models can reflect the normal stresses in the mid-span cross-section because the 20L4 model also owns enough DOFs in terms of normal stresses.

Similarly, normal strains are uniform on the top concrete slab and bottom steel part from Fig. 17. On the steel web, they also show linearity like Fig. 12. For strain analysis, all curves match well with each other, indicating all LE models are effective.

Fig. 18 shows the shear stresses at one-fifth span. Shear stresses are close to zero on the top concrete slab and bottom steel part. The shear stresses mainly occur on the steel web. 20L4 model cannot present great accuracy. 36L9 and 36L16 models are the most effective in shear stress analysis. They show better results than ABAQUS does. Therefore, the ABAQUS model needs mesh refinements on the steel web.

From Fig. 19, shear strains are zero on the top concrete slab and bottom steel part similarly. There is a sharp decrease of shear strains at the interface of steel and concrete, which cannot be seen from the 20L4 and 36L4 models. 36L9 and 36L16 can reflect all curve trends that the ABAQUS model shows. Also, the results from ABAQUS are worse than these of 36L9 and 36L16 models on the steel web, illustrating there is a need for refining meshes of the ABAQUS model in shear strain analysis.

Table 6 shows different results obtained from different models and different cross-sections of the composite box beam. Columns 3 to 5 mean mid-span deflections, normal stresses, and normal strains, respectively. They are all obtained from the bottom nodes which can be seen in Fig. 9(b). Columns 6 to 7 mean one-fifth span shear stresses and strains, respectively. They are all obtained from the middle nodes which can also be found in Fig. 9(b). In terms of mid-span normal stresses and normal strains, the results of LE models are close to these of the ABAQUS model. The differences between LE models and the ABAQUS model are all below 2%. For shear stresses and strains in one-fifth span, results of 36L9 and 36L16 models are relatively different from these of

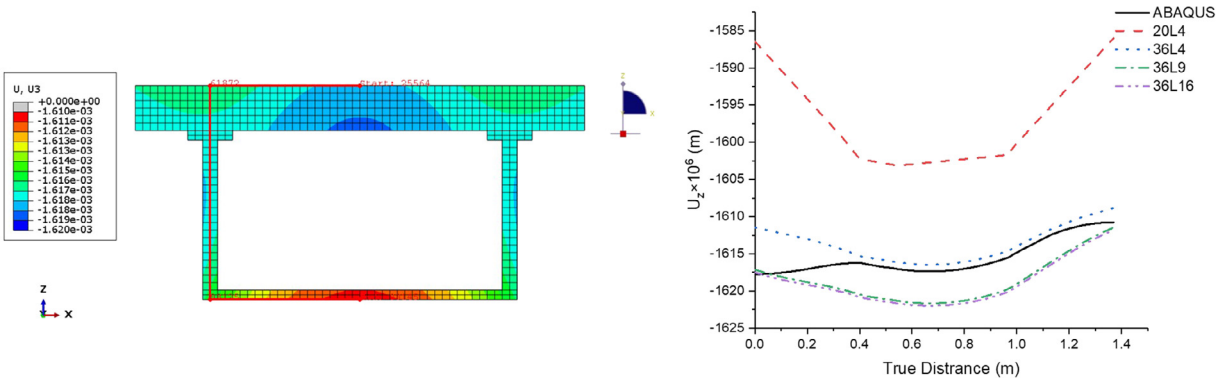

Fig. 15. Mid-span deflections U_z according to different LE-CUF models and 3D ABAQUS.

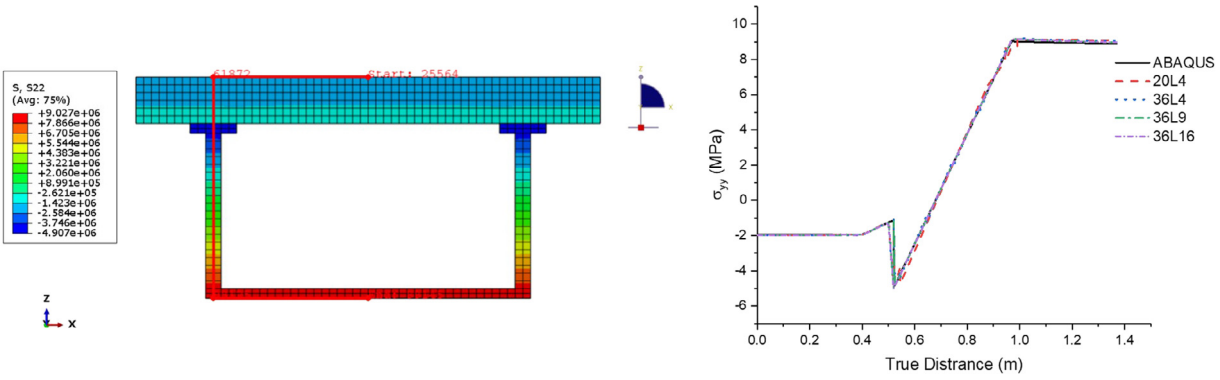

Fig. 16. Mid-span normal stresses σ_{yy} according to different LE-CUF models and 3D ABAQUS.

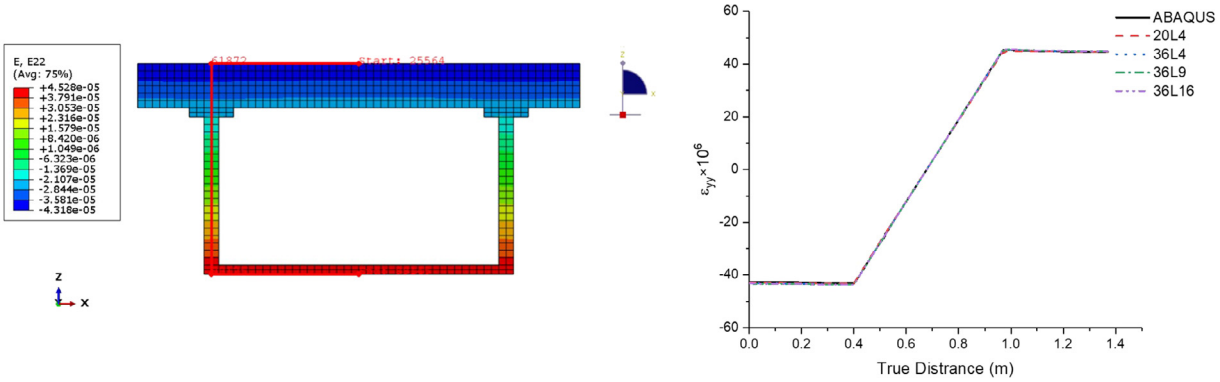

Fig. 17. Mid-span normal strains ϵ_{yy} according to different LE-CUF models and 3D ABAQUS.

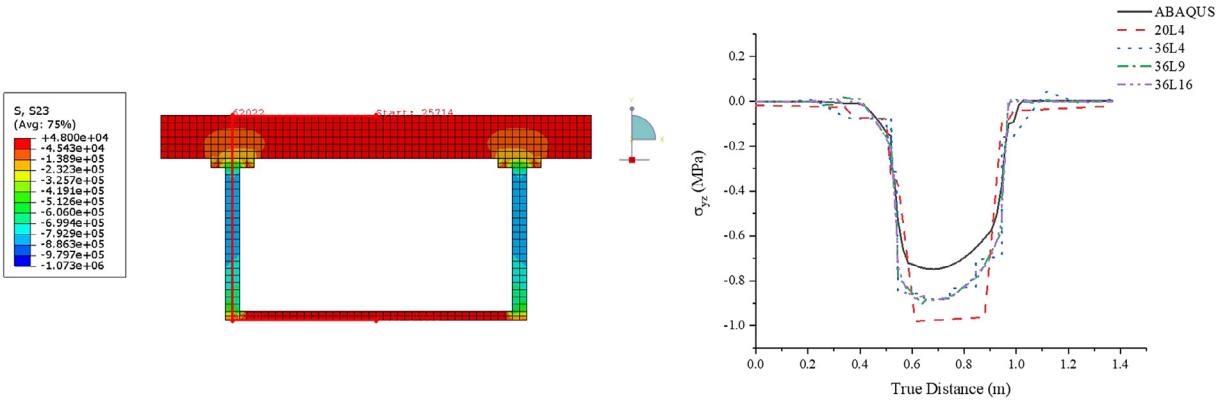

Fig. 18. One-fifth span shear stresses σ_{yz} according to different LE-CUF models and 3D ABAQUS.

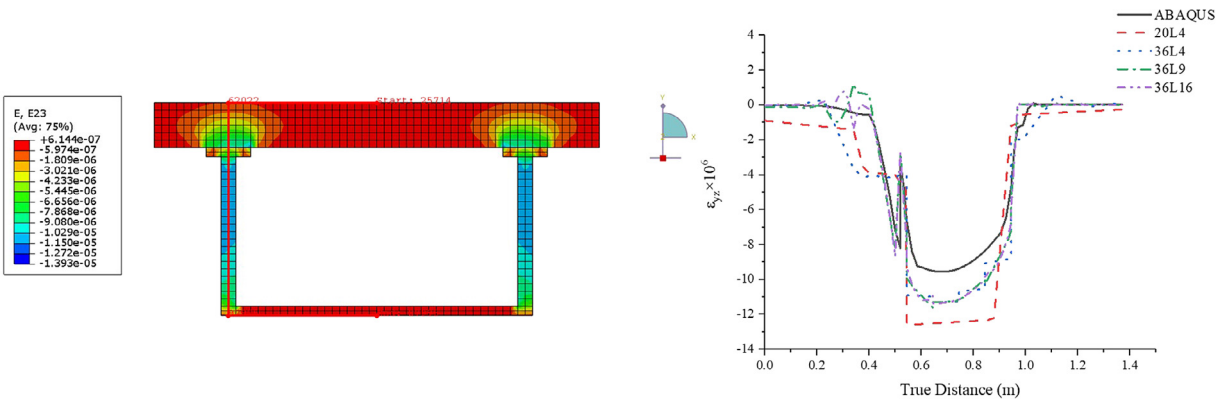

Fig. 19. One-fifth span shear strains ϵ_{yz} according to different LE-CUF models and 3D ABAQUS.

Table 6
Static results of steel–concrete composite box-beam.

Model	DOFs	U_z/mm	σ_{yy}/Mpa	$\epsilon_{yy} \times 10^6$	σ_{yz}/Mpa	$\epsilon_{yz} \times 10^6$
Present 20L4	108	−1.5860	9.0803	44.6532	−0.9717	−12.4381
Present 36L4	336	−1.6088	9.0352	44.7215	−0.8814	−10.6943
Present 36L9	624	−1.6115	8.9819	44.7968	−0.8780	−11.2335
Present 36L16	1260	−1.6115	8.9720	44.7961	−0.8716	−11.1538
ABQ C3D8	1 070 136	−1.6108	8.8982	44.5819	−0.7327	−9.3781

the ABAQUS model, which can be attributed to the non-convergence of the ABAQUS model.

Overall, Figs. 15–19 and Table 6 confirm the accuracy of the proposed all LE models in normal stresses and strains of composite box beams. Besides, they verify the accuracy of the proposed 36L9 and 36L16 models in static analysis of composite box beams.

6. Conclusions

In this work, higher-order beam theories based on CUF are applied to free vibration and stress analysis of simply supported steel–concrete composite beams. Three kinds of Lagrange polynomials, which are Four-point (L4), nine-point (L9), and sixteen-point (L16), are applied to discretize the beam cross-sectional kinematics. Two steel–concrete composite beams were analyzed and compared with the numerical results provided by ABAQUS and those available in [32,56]. It was possible to conclude that:

(1) The results show that the present analytical CW formulation can give 3D numerically quasi-exact natural frequencies, modes, and static performances of composite beams correctly.
(2) The main advantage of this method is that it can deal with shear deformation and higher-order effects, such as warping, without any assumption, using the 1D beam formulation. These effects were comparable to the ones provided by a 3D solid FE using ABAQUS.
(3) The L9 approximation provides a lower limit for vibration analysis of composite beams. Also, it provided a good accuracy when compared with ABAQUS with less DOF. This is a computational advantage of CUF when compared with classical beam theories.
(4) For the stress analysis, the L4 approximation of the cross-sectional kinematics is enough to capture similar results to ABAQUS, in this case even with less DOF than the vibration analysis. However, considering ABAQUS may not provide the best solutions, L9 and L16 approximation can even give better results than ABAQUS sometimes.

On-going work is focused on the improvement of this approach, for which the shear-slip relationship between concrete and steel needs to be considered. Also to improve the stress analysis output for design purposes the material non-linear behavior in steel and concrete needs to be implemented.

CRediT authorship contribution statement

J. Shen: Data curation, Investigation, Validation, Visualization, Writing – original draft. **A. Pagani:** Writing – review & editing, Supervision, Software, Resources, Project administration, Funding acquisition, Conceptualization. **M.R.T. Arruda:** Conceptualization, Investigation, Methodology, Supervision, Validation, Writing – review & editing. **E. Carrera:** Writing – review & editing, Supervision, Resources, Methodology, Conceptualization.

Declaration of competing interest

The authors declare the following financial interests/personal relationships which may be considered as potential competing interests: Alfonso Pagani reports financial support was provided by European Research Council.

Acknowledgment

This research has received funding from the European Research Council (ERC) under the European Union's Horizon 2020 research and innovation programme (Grant agreement No. 850437).

Appendix

In the case of isotropic homogeneous material, the components of the linear stiffness matrix $\overline{\mathbf{K}}^{\tau s}$ in Eq. (18) are:

$$
\begin{aligned}
K_{xx}^{\tau s} &= \alpha^2 E_{\tau s}^{66} + E_{\tau_{,x} s_{,x}}^{22} + E_{\tau_{,z} s_{,z}}^{44} \\
K_{xy}^{\tau s} &= \alpha \left(E_{\tau_{,x} s}^{23} - E_{\tau s_{,x}}^{66} \right) \\
K_{xz}^{\tau s} &= E_{\tau_{,z} s_{,x}}^{44} + E_{\tau_{,x} s_{,z}}^{12} \\
K_{yx}^{\tau s} &= \alpha \left(E_{\tau_{,x} s}^{66} - E_{\tau s_{,x}}^{23} \right) \\
K_{yy}^{\tau s} &= \alpha^2 E_{\tau s}^{33} + E_{\tau_{,x} s_{,x}}^{66} + E_{\tau_{,z} s_{,z}}^{55} \\
K_{yz}^{\tau s} &= \alpha \left(E_{\tau_{,z} s}^{55} - E_{\tau s_{,z}}^{13} \right) \\
K_{zx}^{\tau s} &= E_{\tau_{,x} s_{,z}}^{44} + E_{\tau_{,z} s_{,x}}^{12} \\
K_{zy}^{\tau s} &= \alpha \left(E_{\tau_{,z} s}^{13} - E_{\tau s_{,z}}^{55} \right) \\
K_{zz}^{\tau s} &= \alpha^2 E_{\tau s}^{55} + E_{\tau_{,x} s_{,x}}^{44} + E_{\tau_{,z} s_{,z}}^{11}
\end{aligned}
\tag{23}
$$

where generic term $E_{\tau_{,\theta} s_{,\zeta}}^{\alpha\beta}$ is a cross-sectional moment parameter:

$$
E_{\tau_{,\theta} s_{,\zeta}}^{\alpha\beta} = \int_{\Omega} \tilde{C}_{\alpha\beta} F_{\tau,\theta} F_{s_{,\zeta}} \mathrm{d}\Omega \tag{24}
$$

The components of $\overline{\mathbf{M}}^{\tau s}$ in Eq. (18) are:

$$M_{xx}^{\tau s} = M_{yy}^{\tau s} = M_{zz}^{\tau s} = E_{\tau s}^{\rho}$$
$$M_{xy}^{\tau s} = M_{xz}^{\tau s} = M_{yx}^{\tau s} = M_{yz}^{\tau s} = M_{zx}^{\tau s} = M_{zy}^{\tau s} = 0 \tag{25}$$

where generic term $E_{\tau s}^{\rho}$:

$$E_{\tau s}^{\rho} = \int_{\Omega} \rho F_{\tau} F_{s} \, \mathrm{d}\Omega \tag{26}$$

References

[1] H.M. Mackay, P. Gillespie, C. Leluau, Report on the strength of steel I-beams haunched with concrete, Eng. J. Can. 6 (8) (1923) 365–369.
[2] L. Euler, De Curvis Elasticis, Bousquet, Lausanne and Geneva, 1744.
[3] S.P. Timoshenko, On the corrections for shear of the differential equation for transverse vibrations of prismatic bars, Lond. Edinburgh Dublin Philos. Mag. J. Sci. 41 (245) (1921) 744–746.
[4] S.P. Timoshenko, On the transverse vibrations of bars of uniform cross-section, Lond. Edinburgh Dublin Philos. Mag. J. Sci. 43 (253) (1922) 125–131.
[5] E. Carrera, A. Pagani, M. Petrolo, E. Zappino, Recent developments on refined theories for beams with applications, Mech. Eng. Rev. 2 (2) (2015) 1–30.
[6] I.S. Sokolnikoff, Mathematical Theory of Elasticity, Mcgraw-Hill, New York, USA, 1956.
[7] F. Gruttmann, R. Sauer, W. Wagner, Shear stresses in prismatic beams with arbitrary cross-sections, Internat. J. Numer. Methods Engrg. 45 (1999) 865–889.
[8] F. Gruttmann, W. Wagner, Shear correction factors in Timoshenko's beam theory for arbitrary shaped cross-sections, Comput. Mech. 27 (2001) 199–207.
[9] W. Wagner, F. Gruttmann, A displacement method for the analysis of flexural shear stresses in thin-walled isotropic composite beams, Comput. Struct. 80 (24) (2002) 1843–1851.
[10] V.Z. Vlasov, Thin-Walled Elastic Beams, Israel Program for Scientific Translations, Jerusalem, Israel, 1961.
[11] R. El Fatmi, A non-uniform warping theory for beams, C. R. Mach. 335 (8) (2007) 467–474.
[12] R. El Fatmi, Non-uniform warping including the effects of torsion and shear forces. Part I: A general beam theory, Int. J. Solids Struct. 44 (18–19) (2007) 5912–5929.
[13] R. El Fatmi, Non-uniform warping including the effects of torsion and shear forces. Part II: Analytical and numerical applications, Int. J. Solids Struct. 44 (18–19) (2007) 5930–5952.
[14] R. Schardt, D. Heinz, Structural Dynamics. Chap. Vibrations of thin-walled prismatic structures under simultaneous static load using generalized beam theory, 921–927.
[15] K. Yoon, D.N. Kim, P.S. Lee, Nonlinear torsional analysis of 3D composite beams using the extended St. Venant solution, Struct. Eng. Mech. 62 (2017) 33–42.
[16] P. Ladevéze, Nonlinear Computational Structural Mechanics, Springer, ISBN: 978-1-4612-1432-8, 1999.
[17] B. Bognet, F. Bordeu, F. Chinesta, A. Leygue, A. Poitou, Advanced simulation of models defined in plate geometries: 3D solutions with 2D computational complexity, Comput. Methods Appl. Mech. Engrg. (2012) 201–204.
[18] B. Bognet, F. Chinesta, A. Leygue, A. Poitou, Separated representations of 3D elastic solutions in shell geometries, Adv. Model. Simul. Eng. Sci. 1 (1) (2014) 4.
[19] P. Vidal, L. Gallimard, O. Polit, Composite beam finite element based on the proper generalized decomposition, Comput. Struct. (2012) 102–103.
[20] M. Ghorashi, M. Ghorashi, Nonlinear static and stability analysis of composite beams by the variational asymptotic method, Internat. J. Engrg. Sci. 128 (2018) 127–150.
[21] B. Stefan, W. Tomasz, Vibration of steel-concrete composite beams using the Timoshenko beam model, J. Vib. Control 11 (2005) 829–848.
[22] G. Biscontin, A. Morassi, P. Wendel, Vibrations of steel-concrete composite beams, J. Vib. Control 6 (2000) 691–714.
[23] B. Stefan, W. Tomasz, Experimental verification of natural vibration models of steel-concrete composite beams, J. Vib. Control (2010).
[24] B. Niesterowicz, P. Dunaj, B. Stefan, Timoshenko beam model for vibration analysis of composite steel polymer concrete box beams, J. Theoret. Appl. Mech. 58 (3) (2020) 799–810, Warsaw.
[25] I.E.J. Henderson, X.Q. Zhu, B. Uy, O. Mirza, Dynamic behaviour of steel-concrete composite beams with different types of shear connectors. Part I: Experimental study, Eng. Struct. 103 (2015) 298–307.
[26] I.E.J. Henderson, X.Q. Zhu, B. Uy, O. Mirza, Dynamic behaviour of steel-concrete composite beams with different types of shear connectors. Part II: Modelling and comparison, Eng. Struct. 103 (2015) 308–317.
[27] C.W. Huang, Y.H. Su, Dynamic characteristics of partial composite beams, Int. J. Struct. Stab. Dyn. 8 (4) (2008) 665e685.
[28] Q.H. Nguyen, M. Hjiaj, S. Guezouli, Exact finite element model for shear-deformable two-layer beams with discrete shear connection, Finite Elem. Anal. Des. 47 (7) (2011) 718e727.
[29] Q.H. Nguyen, E. Martinelli, M. Hjiaj, Derivation of the exact stiffness matrix for a two layer Timoshenko beam element with partial interaction, Eng. Struct. 33 (2) (2011) 298e307.
[30] R. Xu, Y.F. Wu, Free vibration and buckling of composite beams with interlayer slip by two-dimensional theory, J. Sound Vib. 313 (3–5) (2008) 875–890.
[31] W. Zhou, L. Jiang, Z. Yu, Analysis of free vibration characteristic of steel-concrete composite box-girder considering shear lag and slip, J. Cent. South Univ. 20 (2013) 2570–2577.
[32] L. Jiang, Z. Lai, W. Zhou, X. Chai1, Natural vibration analysis of steel-concrete composite box beam using improved finite beam element method, Adv. Struct. Eng. 21 (6) (2018) 918–932.
[33] Y. Feng, L. Jiang, W. Zhou, Improved analytical method to investigate the dynamic characteristics of composite box beam with corrugated webs, Int. J. Steel Struct. 20 (1) (2020) 194–206.
[34] Z. Lai, L. Jiang, W. Zhou, X. Chai, Improved finite beam element method to analyze the natural vibration of steel-concrete composite truss beam, Shock Vib., 2017, p. 12, Article ID 5323246.
[35] A. Chakrabarti, A.H. Sheikh, M. Griffith, D.J. Oehlers, Dynamic response of composite beams with partial shear interaction using a higher-order beam theory, J. Struct. Eng. 139 (1) (2013) 47–56.
[36] G. He, D. Wang, X. Yang, Analytical solutions for free vibration and buckling of composite BeamsUsing a higher order BeamTheory, Acta Mech. Solida Sin. 29 (3) (2016).
[37] E. Carrera, G. Giunta, M. Petrolo, Beam Structures: Classical and Advanced Theories, John Wiley and Sons, Chichester, UK, 2011.
[38] E. Carrera, Theories and finite elements for multilayered, anisotropic, composite plates and shells, Arch. Comput. Methods Eng. 9 (2) (2002) 87–140.
[39] E. Carrera, Theories and finite elements for multilayered plates and shells: a unified compact formulation with numerical assessment and benchmarking, Arch. Comput. Methods Eng. 10 (3) (2003) 216–296.
[40] E. Carrera, M. Cinefra, M. Petrolo, E. Zappino, Finite Element Analysis of Structures Through Unified Formulation, John Wiley and Sons, Chichester, UK, 2014.
[41] E. Carrera, G. Giunta, Refined beam theories based on a unified formulation, Int. J. Appl. Mech. 2 (1) (2010) 117–143.
[42] E. Carrera, G. Giunta, P. Nali, M. Petrolo, Refined beam elements with arbitrary cross-section geometries, Comput. Struct. 88 (5–6) (2010) 283–293.
[43] E. Carrera, M. Filippi, Variable kinematic one-dimensional finite elements for the analysis of rotors made of composite materials, J. Eng. Gas Turbines Power 136 (9) (2014) 092501.
[44] G. Giunta, F. Biscani, S. Belouettar, E. Carrera, Analysis of thin-walled beams via a one-dimensional unified formulation through a Navier-type solution, Int. J. Appl. Mech. 3 (3) (2011) 407–434.
[45] E. Carrera, M. Petrolo, Refined one-dimensional formulations for laminated structure analysis, AIAA J. 50 (1) (2012) 176–189.
[46] E. Carrera, M. Petrolo, Refined beam elements with only displacement variables and plate/shell capabilities, Meccanica 47 (3) (2012) 537–556.
[47] A. Pagani, M. Boscolo, J.R. Banerjee, E. Carrera, Exact dynamic stiffness elements based on one-dimensional higher-order theories for free vibration analysis of solid and thin-walled structures, J. Sound Vib. 332 (23) (2013) 6104–6127.
[48] A. Pagani, E. Carrera, M. Boscolo, J.R. Banerjee, Refined dynamic stiffness elements applied to free vibration analysis of generally laminated composite beams with arbitrary boundary conditions, Compos. Struct. 110 (2014) 305–316.
[49] M. Dan, A. Pagani, E. Carrera, Free vibration analysis of simply supported beams with solid and thin-walled cross-sections using higher-order theories based on displacement variables, Thin-Walled Struct. 98 (2016) 478–495.
[50] M. Cinefra, A.G. Miguel, M. Filippi, C. Houriet, A. Pagani, E. Carrera, Homogenization and free-vibration analysis of elastic metamaterial plates by carrera unified formulation finite elements, Mech. Adv. Mater. Struct. 28 (5) (2021) 476–485.
[51] S. Ghazanfari, S. Hamzehei-Javaran, A. Alesadi, S. Shojaee, Free vibration analysis of cross-ply laminated beam structures using refined beam theories and B-spline basis functions, Mech. Adv. Mater. Struct. 28 (5) (2021) 467–475.
[52] M.R.T. Arruda, L.M.S. Castro, A.J.M. Ferreira, Analysis of composite layered beams using carrera unified formulation with Legendre approximation, Composites B 137 (2018) 39–50.
[53] E. Carrera, R. Augello, A. Pagani, X. Xu, Component-wise approach to reinforced concrete structures, Mech. Adv. Mater. Struct. (2021).
[54] ABAQUS analysis user's manual. Version 2016. Dassault Systemes Simulia Corp.
[55] A. Pagani, Strong-Form Governing Equations and Solutions for Variable Kinematic Beam Theories with Practical (Doctoral thesis), University of London applications, City, 2016.
[56] Y. Zhang, Y. Guo, J. Wang, D. Liang, Natural frequency and mode of vibration of steel-concrete composite beam, J. Jilin Univ. Eng. Technol. Ed. 50 (2) (2020) 581–588.